Lawrence Berkeley National Laboratory

LBL Publications

Title

Soft X-Ray Tomography Has Evolved into a Powerful Tool for Revealing Cell Structures

Permalink

https://escholarship.org/uc/item/6v52t3qx

Journal

Annual Review of Analytical Chemistry, 18(1)

ISSN

1936-1327

Authors

Weinhardt, Venera Larabell, Carolyn

Publication Date

2025-03-03

DOI

10.1146/annurey-anchem-071124-093849

Copyright Information

This work is made available under the terms of a Creative Commons Attribution License, available at https://creativecommons.org/licenses/by/4.0/

Peer reviewed

ANNUAL REVIEWS

Annual Review of Analytical Chemistry

Soft X-Ray Tomography Has Evolved into a Powerful Tool for Revealing Cell Structures

Venera Weinhardt^{1,2} and Carolyn Larabell^{2,3,4}

- ¹Centre for Organismal Studies, Heidelberg University, Heidelberg, Germany; email: venera.weinhardt@cos.uni-heidelberg.de
- $^2\mathrm{Molecular}$ Biophysics and Integrated Bioimaging Division, Lawrence Berkeley National Laboratory, Berkeley, California, USA
- ³Department of Anatomy, University of California, San Francisco, California, USA; email: Carolyn.Larabell@ucsf.edu
- ⁴National Center for X-Ray Tomography, Lawrence Berkeley National Laboratory, Berkeley, California, USA



www.annualreviews.org

- · Download figures
- Navigate cited references
- · Keyword search
- Explore related articles
- Share via email or social media

Annu. Rev. Anal. Chem. 2025. 18:427-46

First published as a Review in Advance on March 3, 2025

The Annual Review of Analytical Chemistry is online at anchem.annualreviews.org

https://doi.org/10.1146/annurev-anchem-071124-093849

Copyright © 2025 by the author(s). This work is licensed under a Creative Commons Attribution 4.0 International License, which permits unrestricted use, distribution, and reproduction in any medium, provided the original author and source are credited. See credit lines of images or other third-party material in this article for license information.



Keywords

soft X-ray, cryo-tomography, cell structure, cell types, modeling, segmentation

Abstract

Over the past three decades, soft X-ray tomography (SXT) has rapidly evolved from a proof-of-concept microscopy method into a high-throughput quantitative imaging modality. This advancement enables researchers to address central questions in cell biology. Despite its relatively short developmental period compared to light and electron microscopy, SXT has emerged as a powerful imaging technology. It enables measuring chemical changes in cellular organelles, analyzing three-dimensional structures of whole cells and creating digital cellular models to study cell motility. We discuss the unique nature of SXT to visualize cells without fixation or labeling, enabling quantitative analyses of organelle chemical composition. We explore SXT microscopes available worldwide, SXT segmentation software, and the diverse cell types studied using this technique. We conclude with emerging directions in SXT imaging, including a brief discussion of recent discoveries that are highly influential and likely to become integral to cell biology textbooks.

1. INTRODUCTION

The field of structural cell biology has been transformed in the last few years. On the one hand, single-cell transcriptomics techniques enable profound insight into the nature of cell state and cell identity (1). On the other hand, the latest advancements in imaging techniques have enabled us to visualize complexity across scales from the organization of cells in large tissues to the molecular details inside native cellular environments (2). Apart from an attempt to answer the fundamental question, What are we made of?, insights from structural cell biology have enabled us to modify and reengineer human cells (3) to combat pathogens and diseases.

Several major consortia and initiatives aim at mapping human cells using various methods, including imaging methods, for example, the Human BioMolecular Atlas Program (4), Pancreatic β -Cell Consortium (5), Human Cell Atlas (6), and many others. By providing high-resolution, detailed imaging of cellular structures and processes, microscopy techniques play a crucial role in these initiatives. Over the past two to three decades, the demand for imaging data has surged at an unprecedented rate. During this period, conventional imaging modalities have seen significant advancements, and new techniques, such as soft X-ray tomography (SXT), have been introduced.

The potential of SXT to visualize biological material in the native state at low radiation dosage was theoretically predicted by Sayre et al. in the late 1970s (7). This led to the development of several soft X-ray microscope systems that demonstrated the potential for multiple applications in cell biology research (8–10), with rapid growth at the beginning of the twentieth century due to the development of high-precision X-ray optics (11). Since the construction of the first SXT station dedicated to biological specimens (12), SXT became the method of choice for three-dimensional (3D) imaging of cryo-preserved whole cells, including large mammalian cells.

Similar to medical computed tomography scans, SXT collects a series of two-dimensional (2D) projection images from multiple angles around the specimen. These images are then computationally reconstructed into a 3D volume using algorithms such as filtered back projection or iterative reconstructions (13). The main steps of SXT imaging are depicted in **Figure 1a** and can be summarized as follows (14): (a) harvesting of cells; (b) rapid cryo-fixation to preserve their native state; (c) transfer to the SXT microscope and collection of a series of projection images by rotating the sample; and (d) 3D reconstruction, segmentation, and quantitative analysis of intracellular structures. SXT's ability to penetrate whole cells 20–25 µm in diameter (15), combined with its spatial resolution of 25–60 nm, makes it a valuable tool for studying the anatomy of diverse cells—from bacteria to eukaryotic mouse and human cells—in a near-native state (see examples in **Figure 1b**).

2. THE UNIQUE QUANTITATIVE NATURE OF SOFT X-RAY TOMOGRAPHY

SXT utilizes the natural absorption properties of biological materials in the so-called water window region of the soft X-ray spectrum, which is 284–543 eV or 4.4–2.3 nm. In this energy range, X-rays interact with matter mainly by photoelectric absorption, which is quantitatively defined by the linear absorption coefficient μ (or LAC). By definition, μz is the attenuation of the X-ray beam with intensity I(z) through the thickness of the material z, such that absorption by the specimen is determined by the Beer–Lambert law:

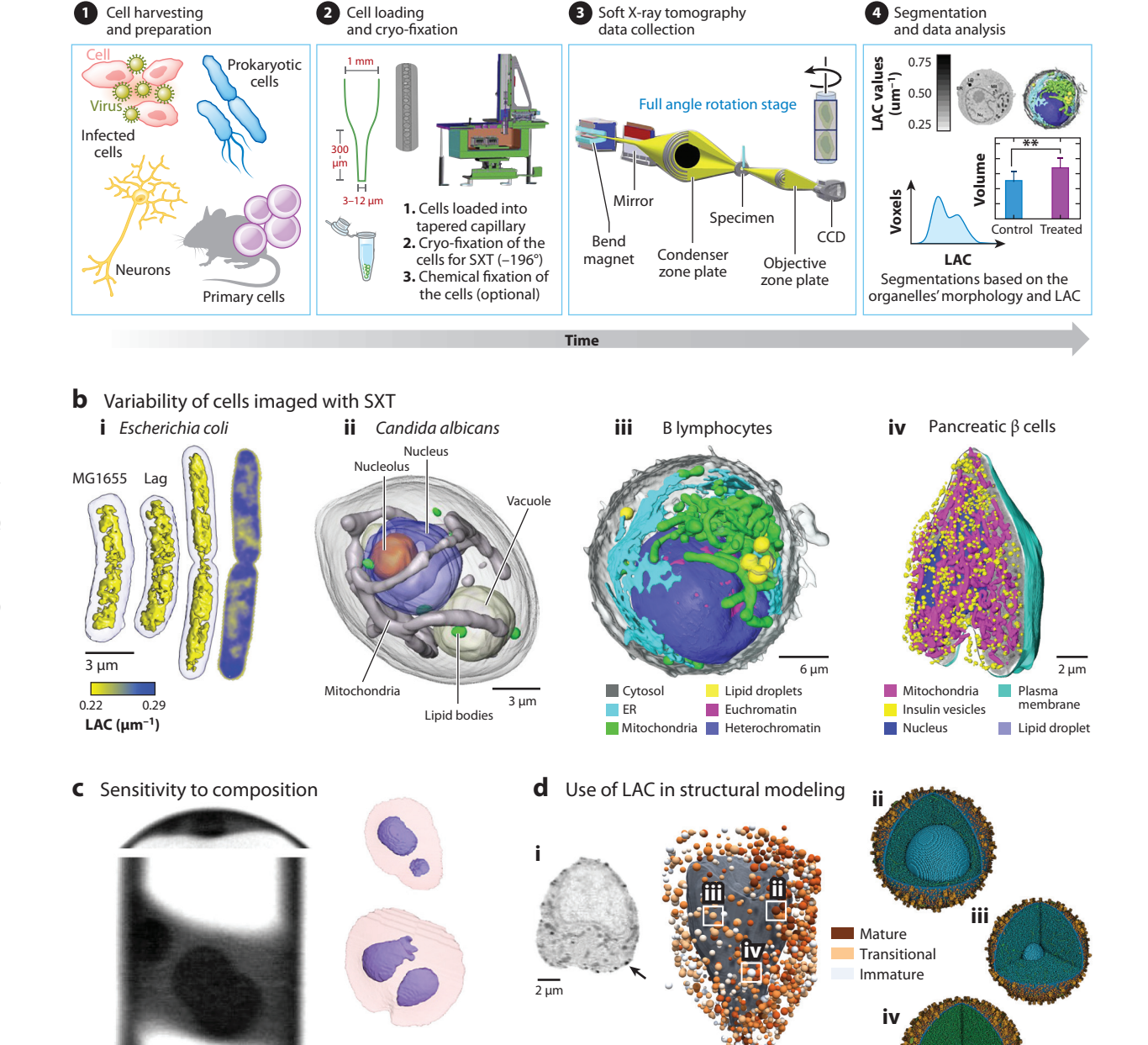
$$I(z) = I_0 e^{-\mu z}$$
.

As other processes of X-ray interaction, such as scattering, are negligible in the water window, the LAC is proportional to the number of atoms per unit area interacting with X-rays (16):

$$\mu \approx \frac{\rho_m N_A}{A},$$

where N_A , ρ_m and A are Avogadro's number, the mass density, and the atomic mass number, respectively.

Therefore, in biological systems, the LAC (μ) is a measure of molecular (e.g., amino acid, carbohydrate, lipid) composition and concentration. The linear dependence of LAC as a function of



Adenine $C_5H_5N_5$ Cytosine $C_4H_5N_3O$

(Caption appears on following page)

Figure 1 (Figure appears on preceding page)

The wide applicability and quantitative nature of SXT. (*a*) The imaging pipeline of SXT imaging starts with the harvesting and preparation of cells ①, which are then loaded into a specimen holder and rapidly frozen to preserve their near-native state ②. SXT is then acquired at cryogenic conditions and reconstructed in 3D volume ③, which with segmentation enables quantitative analysis of cell structure ④. Panel *a* adapted with permission from Reference 14 (CC BY-NC-ND 4.0) (*b*) Selected examples of different cell types visualized with SXT. Panel *i* adapted with permission from Reference 31 (CC BY-NC 4.0); panel *ii* adapted with permission from Reference 140, copyright 2009 National Academy of Sciences; panel *iii* adapted with permission from Reference 14 (CC BY-NC-ND 4.0); panel *iv* adapted from Reference 34 (CC BY 4.0). (*c*) SXT's LAC is sensitive to chemical differences in RNA bases of adenine and cytosine, where adenine has a higher LAC owing to higher carbon and nitrogen contrast. That allows visualization of the 3D distribution of RNA bases in phase-separated structures. Panel *c* adapted with permission from Reference 24 (CC BY-NC-ND 4.0). (*d*, *i*) Pancreatic β cells produce insulin granules (*black arrow*) that undergo different stages of maturation. Combining LAC measurements from SXT data with information on molecular composition from structural biology analysis enabled modeling of (*ii*) mature, (*iii*) transitional, and (*iv*) immature insulin granules in 3D at the level of individual monomers. Panel *i* adapted from Reference 34 (CC BY 4.0); panels *ii-iv* adapted from Reference 29 (CC BY 4.0). Abbreviations: 3D, three-dimensional; CCD, charge-coupled device; ER, endoplasmic reticulum; LAC, linear absorption coefficient; SXT, soft X-ray tomography.

molecular concentration has been confirmed for bovine serum albumin, hemoglobin, and alcohol oxidase crystals (17, 18). It has been extensively used in the analysis of hemoglobin content and structure in cells infected with malaria (19–22).

This quantitative relationship has two implications: (a) organelles that are similar in composition would have similar LAC values, and (b) changes in LAC values are a quantitative measure of a changed organelle's composition. Indeed, if we compare LAC values measured for cells of different origin, e.g., yeast Saccharomyces cerevisiae, green alga Chlamydomonas reinhardtii, pancreatic β cells (INS-1E cell line), and primary mouse cells from olfactory neurons, the organelles involved in the same machinery have similar LAC values. The nucleus in yeast, for example, has typically low absorption values of approximately 0.25 µm⁻¹. The average LAC value of the nucleus is conserved, to the best of our knowledge, for most cell types (Table 1). Measuring the LAC of heterochromatin versus euchromatin in cells from mouse tissue, however, showed that heterochromatin LAC remains constant during differentiation at 0.32 µm⁻¹, while euchromatin LAC increases from 0.18 μ m⁻¹ in stem cells to 0.23 μ m⁻¹ in mature, differentiated cells (18, 23). The sensitivity of LAC at the level of individual nucleobases of RNA also has been demonstrated in vitro (Figure 1c). Though quite similar in chemical composition, the phase separation of adenine and cytosine nucleobases has been analyzed in 3D (24). Having quite opposing functions (25), both chloroplasts and mitochondria are involved in glucose metabolism and synthesis of adenosine triphosphate (ATP) and show LAC values from 0.3 to 0.4 µm⁻¹. The activation of glucose or ATP production was measured by the increase of SXT's LAC in combination with

Table 1 Quantitative analysis of LAC in various cell types

Yeast; Saccaromyces cerevisiae (32)		Green alga; Chlamydomonas reinhardtii (9)		Pancreatic β-cells; INS-1E cell line (35)		Olfactory sensory neurons; primary mouse cells (18)	
Organelle	LAC μm ⁻¹	Organelle	LAC μm ⁻¹	Organelle	LAC μm ⁻¹	Organelle	LAC μm ⁻¹
Vacuole	0.22 ± 0.07	Flagellar roots	0.206	Nucleus (average)	0.26 ± 0.02	Heterochromatin	0.32 ± 0.02
Nucleus	0.26 ± 0.01	Chloroplast	0.385	Mitochondria	0.32 ± 0.02	Euchromatin	0.22 ± 0.02
Nucleolus	0.33 ± 0.01	Pyrenoid	0.441	Insulin vesicles	0.37 ± 0.03	ER	0.24 ± 0.01
Mitochondria	0.36 ± 0.02	Spherical vesicles	0.711	Lipid droplets	0.48-0.90	Mitochondria	0.31 ± 0.02
Lipid bodies	0.55 ± 0.05	NA	NA	NA	NA	Lipid droplets	0.58 ± 0.09

Abbreviations: ER, endoplasmic reticulum; LAC, linear absorption coefficient; NA, not applicable.

other methods in herpes-infected cells (26). Lipids are one of the most absorbing organelles in cells with LACs higher than 0.5 μm^{-1} , likely due to the high carbon concentration. This differential absorption of cellular organelles is an indispensable tool in the segmentation and analysis of organelles' structure.

The molecular information provided by LAC in SXT has become a unique boundary condition to model the interaction of molecules with cells (27, 28). The group of David S. Goodsell has combined the LAC values from SXT with the information from proteomics, structural biology, and cryo-electron microscopy to understand the composition of insulin granules at different stages of maturation (29). By taking known protein structures and modeling the spatial arrangement of these structures to match the distribution of LAC values of insulin granules, the group could model whole insulin granules in three phases of maturation at the monomer level (**Figure 1***d*). This demonstrates the power of LAC values for a variety of organelle analyses. For example, it is now possible to determine the stage of insulin granule maturation after experimental manipulation in unlabeled cells or in tissues obtained from patients. The recent success of artificial intelligence—based protein structure analysis, such as AlphaFold (30), in combination with quantitative information enabled by SXT will make it possible to interpret entire cells at the molecular level.

3. GLOBALIZATION OF SOFT X-RAY TOMOGRAPHY

The unique capabilities of SXT to map the structure of whole cells at the nanometer scale without the need for fixation or staining have led to the construction of six cryogenic SXT stations worldwide (**Figure 2***a*). These stations, located at synchrotron radiation facilities, provide imaging time to the biological community through a peer-reviewed allocation process. Each of these stations offers distinct features and capabilities.

BL09-MISTRAL at ALBA Synchrotron (Spain) combines SXT with spectroscopic analysis and X-ray fluorescence tools for elemental mapping (36, 37). The addition of elemental analysis has been successfully used to understand the interaction of nanoparticles with cells (38–42).

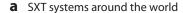
The cryo-SXT station at the Diamond Light Source (United Kingdom) enables correlation with 3D structured illumination microscopy (43, 44), which was recently used to investigate the roles of five viral proteins in virion morphogenesis (45).

Uniquely, the National Center for X-Ray Tomography at the ALS Synchrotron (United States) features the only SXT microscope capable of full-rotation tomography to enable whole-cell imaging and analysis (12). The use of capillaries as sample holders in this station enables automatic alignment of X-ray projection images for 3D reconstructions (13) and application of alternative imaging geometries such as half-acquisition tomography to allow imaging larger specimens with higher resolution optics (15). This capability enables not just a snapshot of the local organelle's structure, but insights into spatial arrangements, such as cell polarization, cross talk between different organelles (35), and detection of rare events in whole cells (46). See **Figure 2***b* for an example of SXT imaging in capillaries.

Further details on beamline parameters of different SXT stations have been summarized elsewhere (47). Recognizing a growing demand for SXT imaging, four additional SXT stations are planned at synchrotron sources. Moreover, there is a continuous development of laboratory or table-top SXT microscopes (**Figure 2***a*,*c*,*d*).

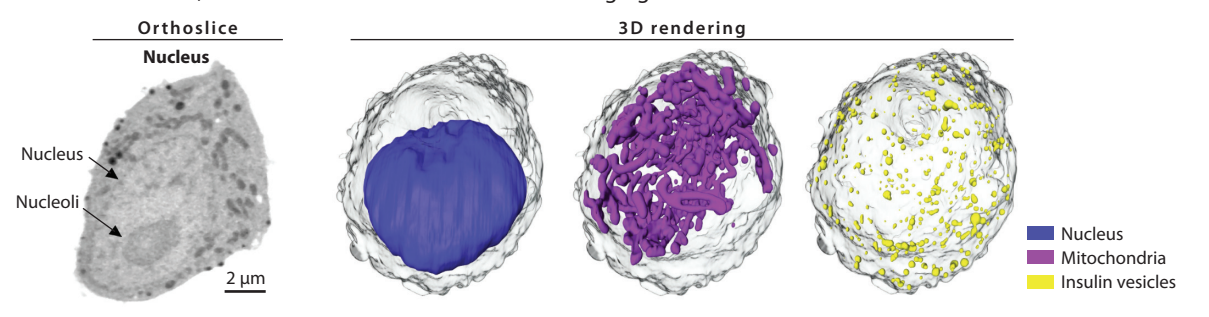
3.1. Transferability to the Laboratory

The first compact water-window soft X-ray microscopes were demonstrated in the late 1990s (49, 50). The ability to achieve images of quality comparable to synchrotron source images and

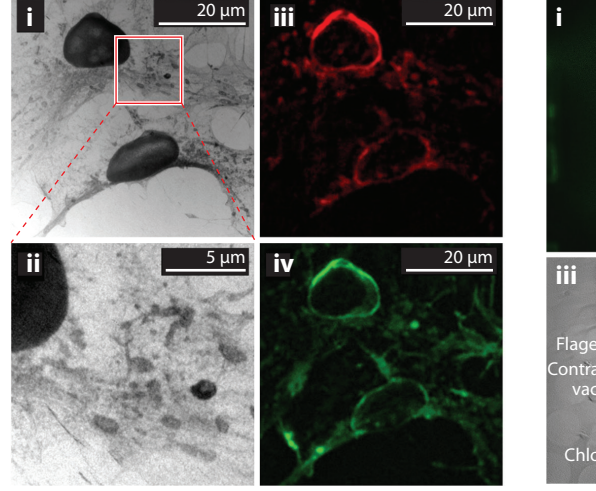




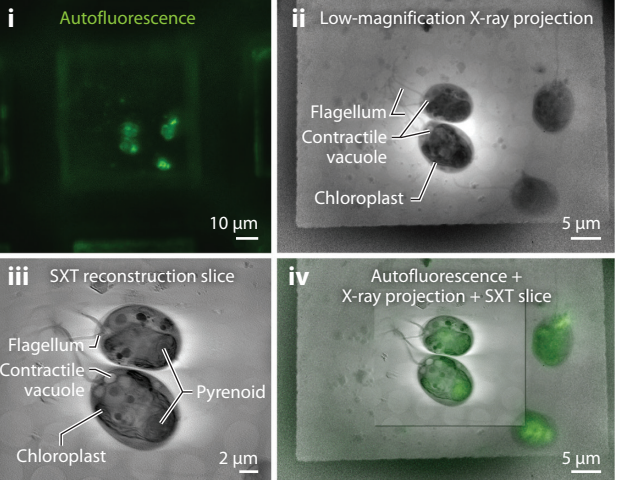
b SXT at NCXT, ALS enables full-rotation whole-cell imaging



c 2D labSXT of dried cells



d 3D labSXT of cryo-preserved cells



(Caption appears on following page)

Figure 2 (Figure appears on preceding page)

Increasing availability of SXT worldwide. (a) World map showing available SXT stations and those under construction at their synchrotron sources and facilities with labSXT systems. (b) Selected example of full-rotation SXT imaging at the NCXT, ALS, in the United States. Virtual slice and 3D renderings of nucleus, mitochondria, and insulin vesicles in pancreatic β cells. Panel b adapted from Reference 35 (CC BY 4.0). (c) SXT and fluorescence images of the monkey kidney fibroblast-like COS-7 cell line from the laboratory-based SXT at Friedrich Schiller University Jena, Germany. (i) 2D soft X-ray projection, showing two nuclei with the surrounding cytoskeleton and mitochondria. (ii) Zoomed-in region of the SXT image highlighted in red frame in panel i with corresponding fluorescence images of (iii) mitochondria and (iv) actin. Panel c adapted from Reference 48 (CC BY 4.0). (d) Chlamydomonas imaged using the SXT-100 by SXT and an integrated visible light fluorescence microscope. (i) Chlamydomonas autofluorescence signal collected with a 0.44-NA 20× objective of the integrated epifluorescence inside the SXT microscope. (ii) Low-magnification X-ray projection featuring four Chlamydomonas cells. (iii) High-magnification, 30-nm-thick virtual slice through an SXT reconstruction of two Chlamydomonas cells. (iv) Correlation and an overlay of images in subpanels i and ii. Samples were provided by Mara Wieser and Prof. Takashi Ishikawa, Paul Scherrer Institute, Switzerland, and imaged with SXT-100 by SiriusXT. Abbreviations: 3D, three-dimensional; ALBA, meaning sunrise in Spanish, is a third-generation synchrotron light source facility in the Barcelona Synchrotron Park, Spain; ALS, Advanced Light Source, Berkeley, California; BESSY II, Berliner Elektronenspeicherring-Gesellschaft für Synchrotronstrahlung, Berlin, Germany; labSXT, laboratory SXT; LNLS, Laboratório Nacional de Luz Síncrotron (Brazilian Synchrotron Light Laboratory), Campinas, Brazil; MAX IV, fourth-generation synchrotron light source facility, Lund, Sweden; NA, numerical aperture; NCXT, National Center for X-Ray Tomography, Berkeley, California; NSLS-II, National Synchrotron Light Source II at Brookhaven National Laboratory, Upton, New York; NSRRC, National Synchrotron Radiation Research Center, Hsinchu Science Park, Hsinchu, China; NSRL, National Synchrotron Radiation Laboratory, Hefei, China; SXT, soft X-ray tomography.

with adequate image acquisition times was demonstrated by Hertz's group (50-52). Since then, the generation and use of water-window X-rays also were shown with laser plasma-based sources based on gas-puff, liquid jet, or solid targets (52-54). The increasing performance of industrial lasers now enables a higher flux of X-rays that is combined with X-ray optics for SXT imaging in research laboratories. These laboratory-based SXT microscopes enable further technical developments of SXT imaging in terms of sample preparation (55), type of detection (56), and correlation with fluorescence microscopy (48) (Figure 2c). Most recently, the laboratory-based SXT has been commercialized by SiriusXT (54). Like synchrotron-based SXT systems, the laboratory SXT-100 microscope enables 3D tomography acquisition of cryogenically preserved cells with 50-nm spatial resolution. The footprint of the microscope is 2 m × 3 m (54). At this time, the laboratorybased microscope enables full tomographic imaging in under 85 min (Figure 2d). Such laboratory systems enable the design and development of correlative imaging, for example, integrated fluorescence microscopy (Figure 2c,d). They are often more versatile microscopes that, owing to unlimited daily availability of X-rays, can push the development of alternative sample preparation strategies, develop new image acquisition strategies, enable imaging in higher-biosafety-level facilities, and investigate new unexplored fields for SXT imaging. Interestingly, the first SXT 2D projection image of a cell using a soft X-ray free electron laser was recently demonstrated (57). Because of the low radiation dose required, this approach might enable SXT imaging of living cells in the future.

The growing number of SXT stations at synchrotron facilities and the development of compact SXT microscopes will broaden access to SXT imaging as well as the development and deployment of this technique to cell biology and many other fields.

3.2. Automatic Analysis of SXT Data

The growing number of available synchrotron and laboratory-based SXT systems and ongoing improvements in throughput of SXT imaging have increased the demand for accelerated image analysis. While tomographic reconstructions are often done automatically, the segmentation of SXT data that is required to analyze structural changes within cells remains primarily a manual task. Images obtained with SXT differ from those generated by light microscopy and electron

microscopy. No heavy stains or fluorescent probes are used in SXT sample preparation, so the differential contrast between organelles is more subtle and like that in the near-native state. Consequently, the contrast difference—based segmentation algorithms developed for electron microscope data are not directly applicable to SXT data.

Several semiautomated and automated segmentation tools have been developed specifically for SXT data. One of the classical approaches to segmentation is the use of gray values of images, e.g., the SXT LAC, to threshold organelles of interest. However, some organelles, such as endoplasmic reticulum and euchromatin, have overlapping LAC values; therefore, Nahas et al. (58) introduced constraints on the size of the organelle into the segmentation software Contour. The software is designed to segment features in the cytoplasm of whole SXT volumes, such as mitochondria, lipid droplets, and vesicles associated with pathological conditions, such as viral infection (**Figure 3a**). The success of deep learning approaches, for instance, segmentation, has not been overlooked by the SXT community. Due to the lack of public SXT data depositories and training datasets for deep learning in the form of segmented volumes, most deep learning tools are organelle- or cell-type-specific. For example, a convolutional neural network (CNN) model for the classification of fused versus partially fused vacuoles based on the labels from fluorescence imaging has been developed for cells of the yeast *S. cerevisiae* (59). Without manual intervention, it enables analysis of vacuole fusion, droplet size (**Figure 3b**), and lipophagy, an important cellular pathway with potential for clearance of misfolded proteins known as hallmarks of degenerative diseases.

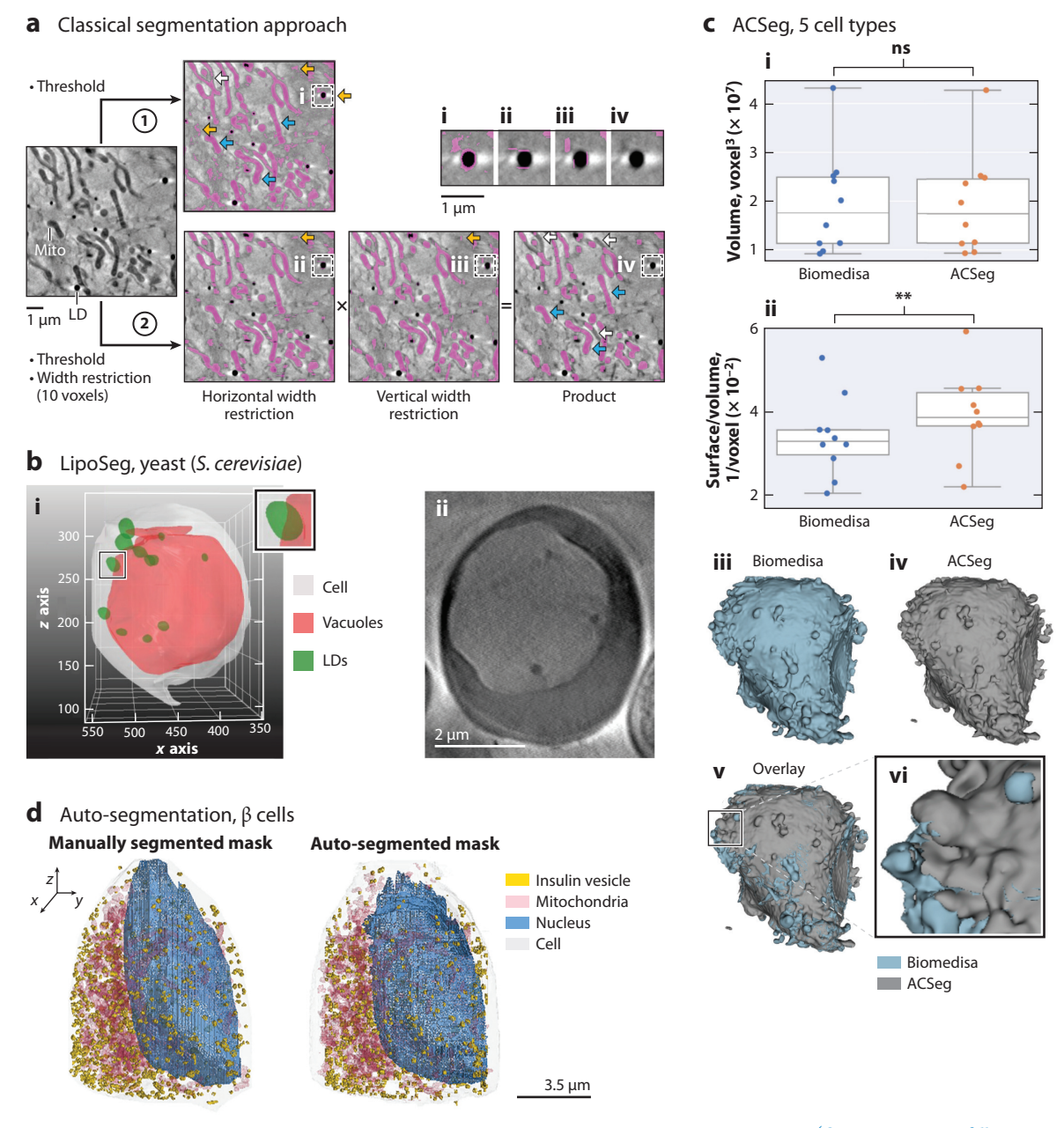
Automatic segmentation of all organelles visible in SXT has been realized for pancreatic β cells. Li et al. (61) developed a two-branch method containing a semantic segmentation branch for categorical masks of mitochondria, nuclei, and cells, and an instance segmentation branch that would separate instances of individual vesicles. By using a priority-based fusion mechanism, the network enables 3D segmentation of organelles in β cells (**Figure 3***d*). This automatic analysis of β cells and their insulin secretion dynamics in conjunction with SXT data on cells from patients will enable new insights into diabetes and the development of potential pharmacological intervention.

Some CNN models have been generalized to automatically segment different cell types (60, 62). Specifically, ACSeg enables segmentation of the cell cytoplasm for five different cell types, with accuracy of more than 95%. This diversification of CNN models is possible through the integration of high-quality training datasets obtained by classical approaches such as random walk, which is more accurate than manual segmentation (e.g., see **Figure 3c**). With the growing attention to statistically significant analyses of cell structure, the development of free and easy-to-use models specifically designed for SXT data will continue to grow. With automatic cell anatomy analysis at hand, SXT imaging allows a wide range of applications.

3.3. SXT Is Nature's Swiss Army Knife for Biological Research

SXT's sensitivity to organic material enables it to address the need for 3D information on organelles and features in any cells, without chemical fixation or staining. SXT imaging has been extensively used to analyze structural changes in response to environmental conditions or mutations in four yeast species (Table 2). A vast number of immortalized cell lines have been used to analyze structural changes upon exposure to external chemicals or objects such as nanoparticles and pathogens. Statistical analysis of publications based on SXT imaging shows that SXT has been used to address phenotypic changes (that is, structural alterations in cellular organelles), nanoparticle–cell interactions, and increasingly since the recent COVID-19 pandemic, viral research on cellular remodeling during infection (Figure 4a and Table 2). Here, we highlight a few emerging directions where SXT could potentially transform the research fields.

One of these fields is focused on understanding membraneless organelles, such as the nucleolus, paraspeckles, nuclear speckles, Cajal bodies, PML bodies, P-bodies, and stress granules, to name a few (63). The family of membraneless organelles continues to expand. These organelles are highly dynamic and by means of phase separation have been shown to regulate transcription, splicing, RNA metabolism with dysregulation of phase transitions linked to neurodegenerative diseases, cancer, and infection biology (64). Many membraneless organelles are small and show



(Caption appears on following page)

Figure 3 (Figure appears on preceding page)

Segmentation pipelines specifically designed for SXT data. (a) Contour semiautomatic segmentation where the mitochondria were segmented based on an intensity threshold (LAC) with a subsequent width restriction to improve labeling quality. The SXT virtual slice is segmented using voxel intensity threshold (blue arrows) and threshold with restriction algorithms to detect mitochondria (magenta). White arrows show areas where mitochondria are missing, and yellow arrows show mislabeling of lipid droplets as mitochondria. Panel a adapted from Reference 58 (CC BY 4.0). (b) CNN-based segmentation of vacuolar shapes in yeast (Saccharomyces cerevisiae) cells. (i) Result of the automatic segmentation of SXT data in panel ii, showing model output after 3D rendering. Panel b adapted with permission from Reference 59 (CC BY-NC-ND 4.0). (c) Quantitative comparison of the cytoplasm segmentation results based on semiautomatic, i.e., Biomedisa, segmentation and a CNN-based model named ACSeg for (i) cell volume and (ii) cell-surface-to-volume ratio. Statistical significances using paired t-test (N = 10): ns, p > 0.05; **, 0.001 \leq 0.01. (iii) Biomedisa (blue) and ACSeg (gray) reconstruction of T cell cytoplasm with accurate cell volume and surface measurements as seen in overlays of two segmentation methods (v and v). Segmentation was accurate on five cell types. Panel v adapted from Reference 60 (CC BY 4.0). (d) Manual and CNN-based automatic segmentation of pancreatic v cells. Panel v adapted from Reference 61 (CC BY 4.0). Abbreviations: CNN, convolutional neural network; LAC, linear absorption coefficient; LD, lipid droplet; SXT, soft X-ray tomography.

complex 3D spatial organization. It is therefore challenging to image them within the crowded structure of whole cells. Owing to the sensitivity to chemical composition, SXT is uniquely positioned to investigate the phase separation of unlabeled proteins in vitro, as demonstrated for the condensation of RNA bases (24).

Recently, condensation-based toxicity of dipeptide repeat polypeptides PR and GR, a leading cause of amyotrophic lateral sclerosis, was studied by SXT in vivo (65). Using machine learning to predict protein condensation, several protein targets were associated with intracellular condensates and tested in vitro. One of these candidates was applied to live bacteria at a concentration that would inhibit a range of pathogens. SXT of these bacteria showed that treated bacteria have compacted nucleoids, measured by LAC, and cytoplasmic condensation (**Figure 4b**), thus confirming that phase separation of bioactive peptides plays a crucial role in vivo. The ability of SXT to probe molecular condensation and cellular structure simultaneously is invaluable in examining the condensate-to-membrane interactions. These insights are of particular interest in understanding what regulates the interactions between molecular condensates and other cellular structures, for example, mitochondria, lipids, or even membranes at the synapse of a neuron. Applied to various cells and types of condensation, SXT will broaden our knowledge and help to establish a bridge for therapeutic interventions targeted to phase separation.

Apart from experimental methods, cells are extensively studied by computational models (66). The development of cellular structural models based on SXT data is beneficial because not only the structure but also the composition of cellular organelles are obtained in 3D. Samuel Isaacson's group used such cellular models to understand the dynamics of proteins required to find specific DNA binding sites (27) and the signaling of proteins enabled by diffusion of proteins through cell cytoplasm toward the nucleus (28). In another study, a comprehensive mathematical model of pancreatic β cell reorganization during glucose-stimulated insulin production was developed through an integrative approach, where SXT data were used to simulate insulin granule trafficking, docking, and exocytosis (67). As mentioned before, by integration of proteomic data with LAC information from SXT (Figure 1d), the composition of the insulin granules at different maturation stages was modeled at single-molecule levels. Apart from physical representations of cell phenotype, such models are unique in modeling interactions with chemical and environmental factors, including signaling and motility of cells. Finally, to understand the motility of parasites such as Plasmodium and Toxoplasma, SXT provided rigid and stereotypical shape models (68) (Figure 4c). The surface models were then used to solve the theoretical model of actin selforganization, which predicts patches of parallel actin filaments circulating up and down a cell to enable bidirectional and unidirectional gliding of parasites. The integration of experimental

Table 2 Representative cells and organisms that have been examined by soft X-ray tomography (SXT) to date^a

Specimen		Specific type with references			
Bacteria		Leptothrix ochracea (9), Escherichia coli (65, 71–77), Mycobacterium smegmatis (71), Salmonella			
		enterica (78), Pseudomonas putida (79), Pseudomonas aeruginosa (80), Staphylococcus aureus (80)			
Yeasts		Saccharomyces cerevisiae (13, 32, 81–84), Saccharomyces pombe (32, 71, 81, 85, 86), Candida albicans			
		(32, 71, 81), Pleurochrysis carterae (87)			
Algae		Chlamydomonas reinhardtii (88), Scenedesmus (89), Chromochloris zofingiensis (90), Ostreococcus tauri			
		(91)			
Plankton		Emiliania huxleyi (92)			
Protozoa		Plasmodium falciparum (20–22), Trypanosoma brucei (93, 94), Toxoplasma gondii (68, 70), Babesia			
		divergens (95)			
Symbiotic species		Magnetotactic holobiont (96)			
Viruses		Vaccinia (97, 98), herpes simplex virus 1 (46, 99–102), hepatitis C (103, 104), reovirus type 3			
		(43), SARS-CoV-2 (33, 105)			
Primary cells		Erythrocytes (106, 107), lymphocytes (78, 81, 99, 108), olfactory sensory neurons (18, 27),			
		myocardial mouse fibroblasts (109), muscle cells from rat aorta (110), human bone marrow			
		(111)			
Immortalized	Human	Embryonic kidney HEK293 (112, 113), malignant melanoma G361 (114), adenocarcinoma			
cell lines		MCF-7 (38-40, 95), hepatocyte-derived cellular carcinoma Huh-7 (104, 109), T lymphoblast			
		CEM (115), fibrosarcoma cell HT1080 (116), colorectal adenocarcinoma HT29 (89),			
		malignant osteosarcoma U2OS (15, 43, 101, 116), fibroblast of foreskin HFF-hTERT cells			
		(101), lymphoblastoid GM12878 (15, 28, 46, 86, 102, 117), lung cancer Calu-3 (33), lung			
		adenocarcinoma A549 (40), A549-ACE2 (33), embryonic human kidney HEK293T-ACE2			
		(33), Jurkat E6–1 T cells (118), osteosarcoma SaOS-2 (119) and MG-63 (41), bone			
		marrow-derived mesenchymal stem cells (120), prostate cancer PC3 (42, 121), colon			
		carcinoma cells HCT-116 (40), hepatocellular carcinoma HeP-G2 (40), colon carcinoma			
		LoVo-S and LoVo-R (122), human skin fibroblasts GM08680/GM18455 (123–125)			
	Mouse	Fibroblasts 3T3 (109, 126–129), basophilic leukemia cell RBL-2H3 (130), macrophage			
		RAW264.7 (131), macrophage-like J774 (126, 129, 132, 133), pheochromocytoma PC12 (93)			
	D:	adenocarcinoma (107, 134), insulinoma INS-1E (34, 35)			
	Pig	Embryonic kidney EFN-R (135)			
	Rabbit	Kidney RK13 (136)			
	Monkey	Fibroblast-like kidney Cos7 (137, 138), epithelial-like kidney BSC-1 (43)			
	Long-nosed	Epithelial kidney PtK2 (36, 97, 139)			
	potoroo Chicken	Embryonic fibroblasts DF1 (97)			
C .1 .: 1: 1		•			
Synthetic biology		RNA condensates (24)			

^aThis table is inspired by and serves as an extension of the previous collection by Harkiolaki et al. (70).

SXT data (e.g., the true structure of cells) and mathematical models to probe and understand phenomena is key to mechanistic explanations or feasible predictions that faithfully recapitulate in vivo situations.

In addition to looking at established and well-understood cells and unicellular organisms, SXT is uniquely positioned to identify new cell types and structures within. Particularly in aquatic biology, SXT has been used to describe the cellular structure of algae, plankton, and symbiotic organisms (**Table 2**). Symbiosis is of particular interest, as it involves the living of two or more species that are dependent on each other in terms of anatomy and metabolism. In the symbiotic relationship between the marine alga *Braarudosphaera bigelowii* and cyanobacterial endosymbiont UCYN-A, SXT has unveiled that the UCYN-A process of replication and division is tightly

synchronized with that of the host algal cell (69). The synchronization of these processes is a hallmark of the transition from an endosymbiont to an organelle. Published as the cover article of the journal *Science*, SXT data show that a single UCYN-A cell is located in each *B. bigelowii* cell. Analysis of hundreds of *B. bigelowii* cells by SXT was used to understand the dynamics of cell-cycle

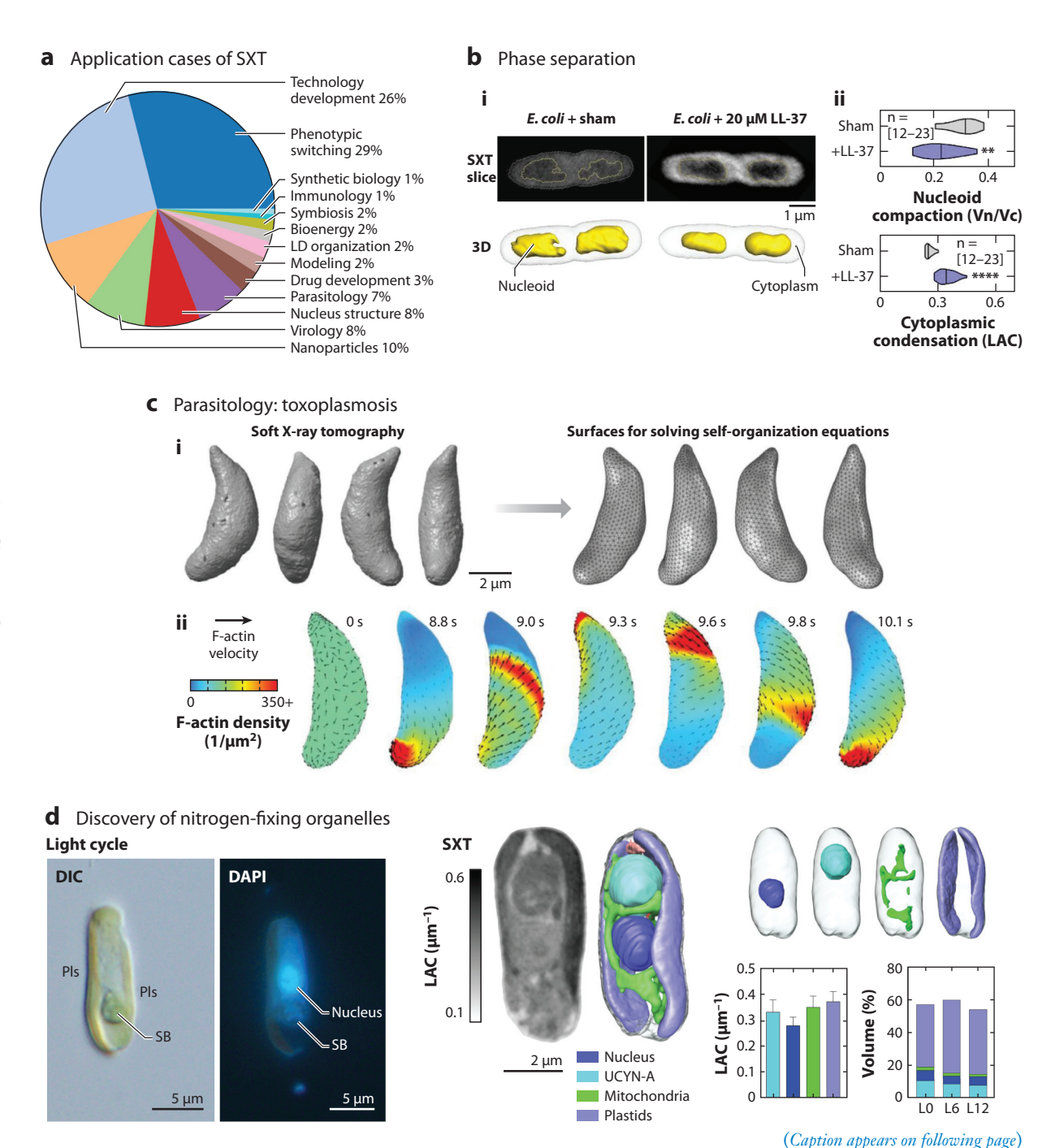


Figure 4 (Figure appears on preceding page)

Selected applications of SXT imaging. (a) Statistical analysis of publications based on SXT data in terms of application field or research question. (b, i) Virtual slices and 3D renderings of E. coli in control cells and after treatment with LL-37 peptide. (ii) Nucleoid compaction is measured as the ratio of nucleoid to cytoplasmic volume, with information on changes in cytoplasmic condensation measured by LAC. Panel b adapted with permission from Reference 65 (CC BY-NC-ND 4.0). (c) Toxoplasma gondii tachyzoite surface rendering of SXT data transferred to triangle-meshed surfaces on which to solve the actin self-organization theoretical model. Panel c adapted with permission from Reference 68 (CC BY-NC-ND 4.0). The geometry of actin patches based on the model is constrained to the surface geometry of T. gondii. (d) Light microscopy images showing a Braarudosphaera bigelowii cell with a UCYN-A SB and Pls. Panel d adapted with permission from Reference 69; copyright 2024 AAAS. Virtual slice and 3D renderings of the same cell with organelles were segmented in 3D and measured in terms of their volume and LAC. Abbreviations: 3D, three-dimensional; DAPI, 4',6-diamidino-2-phenylindole; DIC, differential interference contrast; E. coli, Escherichia coli; LAC, linear attenuation coefficient; LD, lipid droplet; Pls, plastids; SB, spheroid body; SXT, soft X-ray tomography; UCYN-A, Candidatus Atelocyanobacterium thalassa; Vc, volume of cytoplasm; Vn, volume of nucleoid.

changes of UCYN-A in *B. bigelowii* throughout the daily light-dark cycle. Division, which occurs during the dark cycle, was initiated by *B. bigelowii* mitochondria and followed shortly thereafter by the synchronous replication and division of UCYN-A and remaining host organelles. SXT volume and LAC measurements quantified the different steps throughout the cell cycle. These data, combined with the proteomic analysis of the algal host and symbiont, show that UCYN-A serves as a nitrogen-fixing organelle named the nitroplast. This discovery inspires a closer look at other organisms with the potential evolution of symbionts to organelles. With more than 50,000 algae species, marine biology is becoming one of the main directions of SXT imaging.

4. CONCLUSION AND FUTURE PERSPECTIVES

To date, the ability of SXT to visualize whole eukaryotic cells with high resolution and without the need for fixation and staining has been applied to understand hundreds of different cell types. The quantitative measurements of organelle density and high-throughput of volume acquisition are increasingly used to create virtual phenotypic models of cells and their signaling and motility. Due to the large success of SXT in bringing new insights into cell biology, SXT has shifted from an expert-only technology-development domain to a broader use in the biological community. SXT is becoming the method of choice to solve challenging cases of high societal impact.

The number of available SXT microscopes will continue to increase, allowing the SXT method to be adopted by other research fields. A growing number of automatic segmentation algorithms, including deep learning approaches, will enable full automation and quantitative analysis of cell phenotypes, where morphometric data will be linked to genomics, transcriptomics, and proteomics and other methods for cell analysis. The development of these approaches calls for the sharing of SXT data and algorithms in public archives.

In the future, we expect that SXT will continue to improve technologically with further increases in spatial resolution, imaging volume, and throughput. These developments will in turn enable further applications of SXT, for example, the imaging of cells in the context of surrounding extracellular matrix, biomaterials, or tissues.

DISCLOSURE STATEMENT

The authors are not aware of any affiliations, memberships, funding, or financial holdings that might be perceived as affecting the objectivity of this review.

ACKNOWLEDGMENTS

The authors thank Jian-Hua Chen and Valentina Loconte from the National Center for X-Ray Tomography (NCXT) for their assistance in schematics preparation. The authors also thank

SiriusXT for exemplary images obtained with SXT-100 and used in Figure 2d. V.W.'s work was funded within the framework of the Excellence Strategy of the Federal and State Governments of Germany, the Excellence Cluster "3D Matter Made to Order" (3DMM2O), by the CLEXM MSCA-DN project funded by the European Union under Horizon Europe, and by the CoCID project (101017116) funded within the EU Research and Innovation Act. C.L. and the NCXT were supported by the US National Institutes of Health (NIH) National Institute of General Medical Sciences (NIGMS) grant P30GM138441 and US Department of Energy (DOE) Biological and Environmental Research Project DE-AC02-05CH11231.

LITERATURE CITED

- 1. Quake SR. 2021. The cell as a bag of RNA. Trends Genet. 37(12):1064-68
- McCafferty CL, Klumpe S, Amaro RE, Kukulski W, Collinson L, Engel BD. 2024. Integrating cellular electron microscopy with multimodal data to explore biology across space and time. Cell 187(3):563–84
- 3. Deckers J, Anbergen T, Hokke AM, de Dreu A, Schrijver DP, et al. 2023. Engineering cytokine therapeutics. *Nat. Rev. Bioeng.* 1(4):286–303
- 4. Snyder MP, Lin S, Posgai A, Atkinson M, Regev A, et al. 2019. The human body at cellular resolution: the NIH Human Biomolecular Atlas Program. *Nature* 574(7777):187–92
- White KL, McClary K, Singla J, Stevens RC. 2018. Towards generating spatiotemporal multiscale models of human pancreatic beta cells. *Diabetes* 67(Suppl. 1):2171-P
- Regev A, Teichmann SA, Lander ES, Amit I, Benoist C, et al. 2017. Science Forum: The Human Cell Atlas. eLife 6:e27041
- Sayre D, Kirz J, Feder R, Kim DM, Spiller E. 1977. Potential operating region for ultrasoft X-ray microscopy of biological materials. Science 196(4296):1339–40
- Schmahl G, Rudolph D, Niemann B, Christ O. 1980. Zone-plate X-ray microscopy. Q. Rev. Biophys. 13(3):297–315
- Weiß D, Schneider G, Niemann B, Guttmann P, Rudolph D, Schmahl G. 2000. Computed tomography of cryogenic biological specimens based on X-ray microscopic images. *Ultramicroscopy* 84(3):185–97
- Schneider G, Niemann B, Guttmann P, Rudolph D, Schmahl G. 1995. Cryo X-ray microscopy. Synchrotron Radiat. News 8(3):19–28
- Attwood D, Sakdinawat A. 2017. X-Rays and Extreme Ultraviolet Radiation: Principles and Applications. Cambridge, UK: Cambridge Univ. Press. 2nd ed.
- 12. Le Gros MA, McDermott G, Cinquin BP, Smith EA, Do M, et al. 2014. Biological soft X-ray tomography on beamline 2.1 at the Advanced Light Source. *J. Synchrotron Radiat*. 21(Part 6):1370–77
- 13. Parkinson DY, Knoechel C, Yang C, Larabell CA, Le Gros MA. 2012. Automatic alignment and reconstruction of images for soft X-ray tomography. J. Struct. Biol. 177(2):259–66
- Chen J-H, Vanslembrouck B, Loconte V, Ekman A, Cortese M, et al. 2022. A protocol for full-rotation soft X-ray tomography of single cells. STAR Protoc. 3(1):101176
- Ekman A, Chen J-H, Vanslembrouck B, Loconte V, Larabell CA, et al. 2023. Extending imaging volume in soft X-ray tomography. Adv. Photon. Res. 4(4):2200142
- Als-Nielsen J, McMorrow D. 2011. X-rays and their interaction with matter. In *Elements of Modern X-Ray Physics*, ed. J Als-Nielsen, D McMorrow, pp. 1–28. New York: John Wiley & Sons. 2nd ed.
- Hanssen E, Knoechel C, Dearnley M, Dixon MWA, Le Gros M, et al. 2012. Soft X-ray microscopy analysis of cell volume and hemoglobin content in erythrocytes infected with asexual and sexual stages of *Plasmodium falciparum*. 7. Struct. Biol. 177(2):224–32
- Le Gros MA, Clowney EJ, Magklara A, Yen A, Markenscoff-Papadimitriou E, et al. 2016. Soft X-ray tomography reveals gradual chromatin compaction and reorganization during neurogenesis in vivo. *Cell Rep.* 17(8):2125–36
- Hanssen E, Knoechel C, Klonis N, Abu-Bakar N, Deed S, et al. 2011. Cryo transmission X-ray imaging of the malaria parasite, *P. falciparum. J. Struct. Biol.* 173(1):161–68

- Kapishnikov S, Grolimund D, Schneider G, Pereiro E, McNally JG, et al. 2017. Unraveling heme detoxification in the malaria parasite by in situ correlative X-ray fluorescence microscopy and soft X-ray tomography. Sci. Rep. 7(1):7610
- Kapishnikov S, Weiner A, Shimoni E, Guttmann P, Schneider G, et al. 2012. Oriented nucleation of hemozoin at the digestive vacuole membrane in *Plasmodium fulciparum*. PNAS 109(28):11188–93
- Kapishnikov S, Staalsø T, Yang Y, Lee J, Pérez-Berná AJ, et al. 2019. Mode of action of quinoline antimalarial drugs in red blood cells infected by *Plasmodium falciparum* revealed in vivo. *PNAS* 116(46):22946–52
- Ugarte F, Sousae R, Cinquin B, Martin EW, Krietsch J, et al. 2015. Progressive chromatin condensation and H3K9 methylation regulate the differentiation of embryonic and hematopoietic stem cells. Stem Cell Rep. 5(5):728–40
- Boeynaems S, Holehouse AS, Weinhardt V, Kovacs D, Van Lindt J, et al. 2019. Spontaneous driving forces give rise to protein-RNA condensates with coexisting phases and complex material properties. PNAS 116(16):7889–98
- Bölter B, Soll J. 2016. Once upon a time—chloroplast protein import research from infancy to future challenges. Mol. Plant 9(6):798–812
- Leclerc S, Gupta A, Ruokolainen V, Chen J-H, Kunnas K, et al. 2024. Progression of herpesvirus infection remodels mitochondrial organization and metabolism. PLOS Pathog. 20(4):e1011829
- Isaacson SA, Larabell CA, Le Gros MA, McQueen DM, Peskin CS. 2013. The influence of spatial variation in chromatin density determined by X-ray tomograms on the time to find DNA binding sites. *Bull. Math. Biol.* 75(11):2093–117
- Ma J, Do M, Gros MAL, Peskin CS, Larabell CA, et al. 2020. Strong intracellular signal inactivation produces sharper and more robust signaling from cell membrane to nucleus. *PLOS Comput. Biol.* 16(11):e1008356
- 29. Autin L, Barbaro BA, Jewett AI, Ekman A, Verma S, et al. 2022. Integrative structural modelling and visualisation of a cellular organelle. *QRB Discov*. 3:e11
- Jumper J, Evans R, Pritzel A, Green T, Figurnov M, et al. 2021. Highly accurate protein structure prediction with AlphaFold. Nature 596(7873):583–89
- 31. Hammel M, Amlanjyoti D, Reyes FE, Chen J-H, Parpana R, et al. 2016. HU multimerization shift controls nucleoid compaction. *Sci. Adv.* 2(7):e1600650
- 32. Uchida M, Sun Y, McDermott G, Knoechel C, Le Gros MA, et al. 2011. Quantitative analysis of yeast internal architecture using soft X-ray tomography. *Yeast* 28(3):227–36
- 33. Loconte V, Chen J-H, Cortese M, Ekman A, Le Gros MA, et al. 2021. Using soft X-ray tomography for rapid whole-cell quantitative imaging of SARS-CoV-2-infected cells. *Cell Rep. Methods* 1:100117
- 34. White KL, Singla J, Loconte V, Chen J-H, Ekman A, et al. 2020. Visualizing subcellular rearrangements in intact β cells using soft x-ray tomography. *Sci. Adv.* 6(50):eabc8262
- 35. Loconte V, Singla J, Li A, Chen J-H, Ekman A, et al. 2022. Soft X-ray tomography to map and quantify organelle interactions at the mesoscale. *Structure* 30(4):510–21.e3
- Sorrentino A, Nicolás J, Valcárcel R, Chichón FJ, Rosanes M, et al. 2015. MISTRAL: a transmission soft X-ray microscopy beamline for cryo nano-tomography of biological samples and magnetic domains imaging. *J. Synchrotron. Radiat.* 22(4):1112–17
- Valcárcel R, Colldelram C, Gonzalez N, Pereiro E, Pérez-Berná A, Sorrentino A. 2018. New holder for dual-axis cryo soft X-ray tomography of cells at the MISTRAL beamline. In *Proceedings of the Mechanical* Engineering Design of Synchrotron Radiation Equipment and Instrumentation (MEDSI2018), pp. 427–29.
 Paris: JACoW. https://accelconf.web.cern.ch/medsi2018/papers/thph43.pdf
- 38. Conesa JJ, Otón J, Chiappi M, Carazo JM, Pereiro E, et al. 2016. Intracellular nanoparticles mass quantification by near-edge absorption soft X-ray nanotomography. Sci. Rep. 6:22354
- 39. Chiappi M, Conesa JJ, Pereiro E, Sorzano COS, Rodríguez MJ, et al. 2016. Cryo-soft X-ray tomography as a quantitative three-dimensional tool to model nanoparticle:cell interaction. *J. Nanobiotechnol.* 14(1):15
- Kepsutlu B, Wycisk V, Achazi K, Kapishnikov S, Pérez-Berná AJ, et al. 2020. Cells undergo major changes in the quantity of cytoplasmic organelles after uptake of gold nanoparticles with biologically relevant surface coatings. ACS Nano 14(2):2248–64

- Bonany M, Pérez-Berná AJ, Dučić T, Pereiro E, Martin-Gómez H, et al. 2022. Hydroxyapatite nanoparticles-cell interaction: new approaches to disclose the fate of membrane-bound and internalised nanoparticles. *Biomater. Adv.* 142:213148
- 42. Reineck P, Abraham AN, Poddar A, Shukla R, Abe H, et al. 2021. Multimodal imaging and soft X-ray tomography of fluorescent nanodiamonds in cancer cells. *Biotechnol. 7.* 16(3):2000289
- Kounatidis I, Stanifer ML, Phillips MA, Paul-Gilloteaux P, Heiligenstein X, et al. 2020. 3D correlative cryo-structured illumination fluorescence and soft X-ray microscopy elucidates reovirus intracellular release pathway. *Cell* 182(2):515–30.e17
- Okolo CA, Kounatidis I, Groen J, Nahas KL, Balint S, et al. 2021. Sample preparation strategies for efficient correlation of 3D SIM and soft X-ray tomography data at cryogenic temperatures. *Nat. Protoc.* 16(6):2851–85
- 45. Nahas KL, Connor V, Wijesinghe KJ, Barrow HG, Dobbie IM, et al. 2024. Applying 3D correlative structured illumination microscopy and X-ray tomography to characterise herpes simplex virus-1 morphogenesis. bioRxiv 584906. https://doi.org/10.1101/2024.03.13.584906
- Chen J-H, Vanslembrouck B, Ekman A, Aho V, Larabell CA, et al. 2022. Soft X-ray tomography reveals HSV-1-induced remodeling of human B cells. Viruses 14(12):2651
- 47. Okolo CA. 2022. A guide into the world of high-resolution 3D imaging: the case of soft X-ray tomography for the life sciences. *Biochem. Soc. Trans.* 50(2):649–63
- 48. Reinhard J, Kaleta S, Abel JJ, Wiesner F, Wünsche M, et al. 2023. Laboratory-based correlative soft X-ray and fluorescence microscopy in an integrated setup. *Microsc. Microanal.* 29(6):2014–25
- Schmahl G, Niemann B, Rudolph D, Diehl M, Thieme J, et al. 1992. A laboratory X-ray microscope with a plasma X-ray source. In X-Ray Microscopy III, Springer Series in Optical Sciences Vol. 67, ed. AG Michette, GR Morrison, CJ Uckley, pp. 66–69. Berlin/Heidelberg: Springer
- Berglund M, Rymell L, Peuker M, Wilhein T, Hertz HM. 2000. Compact water-window transmission X-ray microscopy. 7. Microsc. 197(3):268–73
- Hertz HM, von Hofsten O, Bertilson M, Vogt U, Holmberg A, et al. 2012. Laboratory cryo soft X-ray microscopy. J. Struct. Biol. 177(2):267–72
- Kördel M, Dehlinger A, Seim C, Vogt U, Fogelqvist E, et al. 2020. Laboratory water-window X-ray microscopy. Optica 7(6):658–74
- Wachulak PW, Torrisi A, Krauze W, Bartnik A, Kostecki J, et al. 2019. A "water window" tomography based on a laser-plasma double-stream gas-puff target soft X-ray source. Appl. Phys. B 125(5):70
- Fahy K, Weinhardt V, Vihinen-Ranta M, Fletcher N, Skoko D, et al. 2021. Compact Cell Imaging Device (CoCID) to provide insights into the cellular origins of viral infections. J. Phys. Photon. 3:031002
- Chatzimpinou A, Funaya C, Rogers D, O'Connor S, Kapishnikov S, et al. 2023. Dehydration as alternative sample preparation for soft X-ray tomography. J. Microsc. 291(3):248–55
- Osuchowska PN, Wachulak P, Nowak-Stępniowska A, Bartnik A, Gnanachandran K, et al. 2020. Imaging of cell structures using optimized soft X-ray contact microscopy. Appl. Sci. 10(19):6895
- 57. Egawa S, Sakurai K, Takeo Y, Yoshinaga K, Takei M, et al. 2024. Observation of mammalian living cells with femtosecond single pulse illumination generated by a soft X-ray free electron laser. Optica 11(6):736–43
- 58. Nahas KL, Fernandes JF, Crump C, Graham S, Harkiolaki M. 2022. *Contour*: a semi-automated segmentation and quantitation tool for cryo-soft-X-ray tomography. *Biol. Imaging* 2:e3
- Egebjerg JM, Szomek M, Thaysen K, Juhl AD, Kozakijevic S, et al. 2023. Automated quantification of vacuole fusion and lipophagy in *Saccharomyces cerevisiae* from fluorescence and cryo-soft X-ray microscopy data using deep learning. *Autophagy* 20(4):902–22
- Erozan A, Lösel PD, Heuveline V, Weinhardt V. 2024. Automated 3D cytoplasm segmentation in soft X-ray tomography. iScience 27(6):109856
- 61. Li A, Zhang X, Singla J, White K, Loconte V, et al. 2022. Auto-segmentation and time-dependent systematic analysis of mesoscale cellular structure in β-cells during insulin secretion. PLOS ONE 17(3):e0265567
- 62. Dyhr MCA, Sadeghi M, Moynova R, Knappe C, Kepsutlu B, et al. 2022. 3D-surface reconstruction of cellular cryo-soft X-ray microscopy tomograms using semi-supervised deep learning. *PNAS* 120(24):e2209938120

- 63. Hirose T, Ninomiya K, Nakagawa S, Yamazaki T. 2023. A guide to membraneless organelles and their various roles in gene regulation. *Nat. Rev. Mol. Cell Biol.* 24(4):288–304
- Wang B, Zhang L, Dai T, Qin Z, Lu H, et al. 2021. Liquid–liquid phase separation in human health and diseases. Signal Transduct. Target. Ther. 6:290
- Boeynaems S, Ma XR, Yeong V, Ginell GM, Chen J-H, et al. 2023. Aberrant phase separation is a common killing strategy of positively charged peptides in biology and human disease. bioRxiv 531820. https://doi.org/10.1101/2023.03.09.531820
- Loconte V, Chen J-H, Vanslembrouck B, Ekman AA, McDermott G, et al. 2023. The role of soft X-ray tomography in generating whole-cell models. *Microsc. Microanal.* 29(Suppl. 1):1170
- Raveh B, Sun L, White KL, Sanyal T, Tempkin J, et al. 2021. Bayesian metamodeling of complex biological systems across varying representations. PNAS 118(35):e2104559118
- Hueschen CL, Zarko LS, Chen J-H, LeGros MA, Larabell CA, et al. 2022. Emergent actin flows explain diverse parasite gliding modes. bioRxiv 495399. https://doi.org/10.1101/2022.06.08.495399
- Coale TH, Loconte V, Turk-Kubo KA, Vanslembrouck B, Mak WKE, et al. 2024. Nitrogen-fixing organelle in a marine alga. Science 384(6692):217–22
- 70. Harkiolaki M, Darrow MC, Spink MC, Kosior E, Dent K, Duke E. 2018. Cryo-soft X-ray tomography: using soft X-rays to explore the ultrastructure of whole cells. *Emerg. Top. Life Sci.* 2(1):81–92
- McDermott G, Fox DM, Epperly L, Wetzler M, Barron AE, et al. 2012. Visualizing and quantifying cell phenotype using soft X-ray tomography. *Bioessays* 34(4):320–27
- Le Gros MA, McDermott G, Uchida M, Knoechel CG, Larabell CA. 2009. High-aperture cryogenic light microscopy. J. Microsc. 235(1):1–8
- 73. Cossa A, Trépout S, Wien F, Groen J, Le Brun E, et al. 2022. Cryo soft X-ray tomography to explore Escherichia coli nucleoid remodeling by Hfq master regulator. J. Struct. Biol. 214(4):107912
- Remesh SG, Verma SC, Chen J-H, Ekman AA, Larabell CA, et al. 2020. Nucleoid remodeling during environmental adaptation is regulated by HU-dependent DNA bundling. *Nat. Commun.* 11(1):2905
- Mehta AP, Supekova L, Chen J-H, Pestonjamasp K, Webster P, et al. 2018. Engineering yeast endosymbionts as a step toward the evolution of mitochondria. PNAS 115(46):11796–801
- Chongsiriwatana NP, Lin JS, Kapoor R, Wetzler M, Rea JAC, et al. 2017. Intracellular biomass flocculation as a key mechanism of rapid bacterial killing by cationic, amphipathic antimicrobial peptides and peptiods. Sci. Rep. 7:16718
- Cossa A, Wien F, Turbant F, Kaczorowski T, Węgrzyn G, et al. 2022. Evaluation of the role of bacterial
 amyloid on nucleoid structure using cryo-soft X-ray tomography. In *Bacterial Amyloids: Methods and*Protocols, ed. V Arluison, F Wien, A Marcoleta, pp. 319–33. New York: Springer
- Cruz-Adalia A, Ramirez-Santiago G, Calabia-Linares C, Torres-Torresano M, Feo L, et al. 2014. T
 cells kill bacteria captured by transinfection from dendritic cells and confer protection in mice. *Cell Host Microbe* 15(5):611–22
- Eng T, Banerjee D, Menasalvas J, Chen Y, Gin J, et al. 2023. Ensemble and iterative engineering for maximized bioconversion to the blue pigment, indigoidine from non-canonical sustainable carbon sources. *Cell Rep.* 42(9):113087
- Linklater DP, Le Guével X, Bryant G, Baulin VA, Pereiro E, et al. 2022. Lethal interactions of atomically
 precise gold nanoclusters and *Pseudomonas aeruginosa* and *Staphylococcus aureus* bacterial cells. ACS Appl.
 Mater. Interfaces 14(28):32634–45
- Larabell CA, Nugent KA. 2010. Imaging cellular architecture with X-rays. Curr. Opin. Struct. Biol. 20(5):623–31
- Sontag EM, Morales-Polanco F, Chen J-H, McDermott G, Dolan PT, et al. 2023. Nuclear and cytoplasmic spatial protein quality control is coordinated by nuclear–vacuolar junctions and perinuclear ESCRT. Nat. Cell Biol. 25(5):699–713
- Walters AD, Amoateng K, Wang R, Chen J-H, McDermott G, et al. 2019. Nuclear envelope expansion in budding yeast is independent of cell growth and does not determine nuclear volume. *Mol. Biol. Cell* 30(1):131–45
- 84. Jamme F, Cinquin B, Gohon Y, Pereiro E, Réfrégiers M, Froissard M. 2020. Synchrotron multimodal imaging in a whole cell reveals lipid droplet core organization. *J. Synchrotron Radiat*. 27(Part 3):772–78

- 85. Smith EA, Cinquin BP, Do M, McDermott G, Le Gros MA, Larabell CA. 2014. Correlative cryogenic tomography of cells using light and soft x-rays. *Ultramicroscopy* 143:33–40
- Weinhardt V, Chen J-H, Ekman AA, Guo J, Remesh SG, et al. 2020. Switchable resolution in soft x-ray tomography of single cells. PLOS ONE 15(1):e0227601
- 87. Gal A, Sorrentino A, Kahil K, Pereiro E, Faivre D, Scheffel A. 2018. Native-state imaging of calcifying and noncalcifying microalgae reveals similarities in their calcium storage organelles. *PNAS* 115(43):11000–5
- Hummel E, Guttmann P, Werner S, Tarek B, Schneider G, et al. 2012. 3D ultrastructural organization of whole *Chlamydomonas reinhardtii* cells studied by nanoscale soft X-ray tomography. *PLOS ONE* 7(12):e53293
- 89. Otón J, Pereiro E, Conesa JJ, Chichón FJ, Luque D, et al. 2017. XTEND: extending the depth of field in cryo soft X-ray tomography. *Sci. Rep.* 7:45808
- Roth MS, Gallaher SD, Westcott DJ, Iwai M, Louie KB, et al. 2019. Regulation of oxygenic photosynthesis during trophic transitions in the green alga Chromochloris zofingiensis. Plant Cell 31(3):579-601
- Smallwood CR, Chrisler W, Chen J-H, Patello E, Thomas M, et al. 2018. Ostreococcus tauri is a highlipid content green algae that extrudes clustered lipid droplets. bioRxiv 249052. https://doi.org/10. 1101/249052
- 92. Sviben S, Gal A, Hood MA, Bertinetti L, Politi Y, et al. 2016. A vacuole-like compartment concentrates a disordered calcium phase in a key coccolithophorid alga. *Nat. Commun.* 7(1):11228
- Luengo I, Darrow MC, Spink MC, Sun Y, Dai W, et al. 2017. SuRVoS: Super-Region Volume Segmentation workbench. J. Struct. Biol. 198(1):43–53
- Cesaro G, Hiraiwa PM, Carneiro FRG, Rouam V, Legrand P, et al. 2020. Downregulation of the essential Rrp44 ribonuclease causes extensive ultra-structure cell modifications in *Trypanosoma brucei*. bioRxiv 971424. https://doi.org/10.1101/2020.02.29.971424
- Conesa JJ, Sevilla E, Terrón MC, González LM, Gray J, et al. 2020. Four-dimensional characterization of the *Babesia divergens* asexual life cycle, from the trophozoite to the multiparasite stage. mSphere 5(5):e00928-20
- Chevrier DM, Juhin A, Menguy N, Bolzoni R, Soto-Rodriguez PED, et al. 2023. Collective magnetotaxis
 of microbial holobionts is optimized by the three-dimensional organization and magnetic properties of
 ectosymbionts. PNAS 120(10):e2216975120
- 97. Chichón FJ, Rodríguez MJ, Pereiro E, Chiappi M, Perdiguero B, et al. 2012. Cryo X-ray nano-tomography of vaccinia virus infected cells. *7. Struct. Biol.* 177(2):202–11
- Carrascosa JL, Chichón FJ, Pereiro E, Rodríguez MJ, Fernández JJ, et al. 2009. Cryo-X-ray tomography of vaccinia virus membranes and inner compartments. J. Struct. Biol. 168(2):234–39
- 99. Myllys M, Ruokolainen V, Aho V, Smith EA, Hakanen S, et al. 2016. Herpes simplex virus 1 induces egress channels through marginalized host chromatin. Sci. Rep. 6:28844
- Aho V, Myllys M, Ruokolainen V, Hakanen S, Mäntylä E, et al. 2017. Chromatin organization regulates viral egress dynamics. Sci. Rep. 7:3692
- Nahas KL, Connor V, Harkiolaki M, Crump CM, Graham SC. 2021. Near-native state imaging by cryosoft-X-ray tomography reveals remodelling of cytoplasmic vesicles and mitochondria during HSV-1 infection. PLOS Pathog. 18(7):e1010629
- Aho V, Mäntylä E, Ekman A, Hakanen S, Mattola S, et al. 2019. Quantitative microscopy reveals stepwise alteration of chromatin structure during herpesvirus infection. Viruses 11(10):935
- Pérez-Berná AJ, Rodríguez MJ, Chichón FJ, Friesland MF, Sorrentino A, et al. 2016. Structural changes in cells imaged by soft X-ray cryo-tomography during hepatitis C virus infection. ACS Nano 10(7):6597–611
- 104. Perez-Berna AJ, Benseny-Cases N, Rodríguez MJ, Valcarcel R, Carrascosa JL, et al. 2021. Monitoring reversion of hepatitis C virus-induced cellular alterations by direct-acting antivirals using cryo soft X-ray tomography and infrared microscopy. Acta Crystallogr. D Struct. Biol. 77(Part 11):1365–77
- Mendonca L, Howe A, Gilchrist JB, Sun D, Knight M, et al. 2020. SARS-CoV-2 assembly and egress pathway revealed by correlative multi-modal multi-scale cryo-imaging. bioRxiv 370239. https://doi. org/10.1101/2020.11.05.370239

- 106. Darrow MC, Zhang Y, Cinquin BP, Smith EA, Boudreau R, et al. 2016. Visualizing red blood cell sickling and the effects of inhibition of sphingosine kinase 1 using soft X-ray tomography. J. Cell Sci. 129(18):3511–17
- McDermott G, Le Gros MA, Larabell CA. 2012. Visualizing cell architecture and molecular location using soft X-ray tomography and correlated cryo-light microscopy. Annu. Rev. Phys. Chem. 63:225–39
- Smith EA, McDermott G, Do M, Leung K, Panning B, et al. 2014. Quantitatively imaging chromosomes by correlated cryo-fluorescence and soft X-ray tomographies. *Biophys.* 7. 107(8):1988–96
- Groen J, Palanca A, Aires A, Conesa JJ, Maestro D, et al. 2021. Correlative 3D cryo X-ray imaging reveals intracellular location and effect of designed antifibrotic protein-nanomaterial hybrids. *Chem. Sci.* 12(45):15090–103
- 110. Polo CC, Fonseca-Alaniz MH, Chen J-H, Ekman A, McDermott G, et al. 2020. Three-dimensional imaging of mitochondrial cristae complexity using cryo-soft X-ray tomography. *Sci. Rep.* 10:21045
- Procopio A, Malucelli E, Pacureanu A, Cappadone C, Farruggia G, et al. 2019. Chemical fingerprint of Zn-hydroxyapatite in the early stages of osteogenic differentiation. ACS Cent. Sci. 5(8):1449–60
- Duke EMH, Razi M, Weston A, Guttmann P, Werner S, et al. 2014. Imaging endosomes and autophagosomes in whole mammalian cells using correlative cryo-fluorescence and cryo-soft X-ray microscopy (cryo-CLXM). *Ultramicroscopy* 143:77–87
- Duke E, Dent K, Razi M, Collinson LM. 2014. Biological applications of cryo-soft X-ray tomography. 7. Microsc. 255(2):65–70
- Carzaniga R, Domart M-C, Duke E, Collinson LM. 2014. Correlative cryo-fluorescence and cryo-soft X-ray tomography of adherent cells at European synchrotrons. Methods Cell Biol. 124:151–78
- Ramírez-Santiago G, Robles-Valero J, Morlino G, Cruz-Adalia A, Pérez-Martínez M, et al. 2016.
 Clathrin regulates lymphocyte migration by driving actin accumulation at the cellular leading edge. *Eur. 7. Immunol.* 46(10):2376–87
- Ekman AA, Chen J-H, Guo J, McDermott G, Le Gros MA, Larabell CA. 2017. Mesoscale imaging with cryo-light and X-rays: larger than molecular machines, smaller than a cell. *Biol. Cell* 109(1):24–38
- Ekman A, Weinhardt V, Chen J-H, McDermott G, Le Gros MA, Larabell C. 2018. PSF correction in soft X-ray tomography. J. Struct. Biol. 204(1):9–18
- Rojas-Gómez A, Dosil SG, Chichón FJ, Fernández-Gallego N, Ferrarini A, et al. 2023. Chaperonin CCT controls extracellular vesicle production and cell metabolism through kinesin dynamics. J. Extracell. Vesicles 12(6):12333
- Rossi F, Picone G, Cappadone C, Sorrentino A, Columbaro M, et al. 2023. Shedding light on osteosarcoma cell differentiation: impact on biomineralization and mitochondria morphology. *Int. J. Mol. Sci.* 24(10):8559
- Sorrentino A, Malucelli E, Rossi F, Cappadone C, Farruggia G, et al. 2021. Calcite as a precursor of hydroxyapatite in the early biomineralization of differentiating human bone-marrow mesenchymal stem cells. *Int. 7. Mol. Sci.* 22(9):4939
- Poddar A, Conesa JJ, Liang K, Dhakal S, Reineck P, et al. 2019. Encapsulation, visualization and expression of genes with biomimetically mineralized zeolitic imidazolate framework-8 (ZIF-8). Small 15(36):1902268
- 122. Moscheni C, Malucelli E, Castiglioni S, Procopio A, De Palma C, et al. 2019. 3D quantitative and ultrastructural analysis of mitochondria in a model of doxorubicin sensitive and resistant human colon carcinoma cells. *Cancers* 11(9):1254
- 123. Wüstner D, Juhl AD, Egebjerg JM, Werner S, McNally J, Schneider G. 2023. Kinetic modelling of sterol transport between plasma membrane and endo-lysosomes based on quantitative fluorescence and X-ray imaging data. Front. Cell Dev. Biol. 11:1144936
- 124. Juhl AD, Heegaard CW, Werner S, Schneider G, Krishnan K, et al. 2021. Quantitative imaging of membrane contact sites for sterol transfer between endo-lysosomes and mitochondria in living cells. Sci. Rep. 11:8927
- 125. Juhl AD, Lund FW, Jensen MLV, Szomek M, Heegaard CW, et al. 2021. Niemann Pick C2 protein enables cholesterol transfer from endo-lysosomes to the plasma membrane for efflux by shedding of extracellular vesicles. *Chem. Phys. Lipids* 235:105047

- Büchner T, Drescher D, Merk V, Traub H, Guttmann P, et al. 2016. Biomolecular environment, quantification, and intracellular interaction of multifunctional magnetic SERS nanoprobes. *Analyst* 141(17):5096–106
- 127. McDermott G, Le Gros MA, Knoechel CG, Uchida M, Larabell CA. 2009. Soft X-ray tomography and cryogenic light microscopy: the cool combination in cellular imaging. *Trends Cell Biol.* 19(11):587–95
- Živanović V, Seifert S, Drescher D, Schrade P, Werner S, et al. 2019. Optical nanosensing of lipid accumulation due to enzyme inhibition in live cells. ACS Nano 13(8):9363–75
- 129. Drescher D, Büchner T, Guttmann P, Werner S, Schneider G, Kneipp J. 2019. X-ray tomography shows the varying three-dimensional morphology of gold nanoaggregates in the cellular ultrastructure. *Nanoscale Adv.* 1(8):2937–45
- 130. Chen H-Y, Chiang DM-L, Lin Z-J, Hsieh C-C, Yin G-C, et al. 2016. Nanoimaging granule dynamics and subcellular structures in activated mast cells using soft X-ray tomography. *Sci. Rep.* 6:34879
- 131. Varsano N, Dadosh T, Kapishnikov S, Pereiro E, Shimoni E, et al. 2016. Development of correlative cryo-soft X-ray tomography and stochastic reconstruction microscopy. A study of cholesterol crystal early formation in cells. *J. Am. Chem. Soc.* 138(45):14931–40
- Varsano N, Beghi F, Dadosh T, Elad N, Pereiro E, et al. 2019. The effect of the phospholipid bilayer environment on cholesterol crystal polymorphism. ChemPlusChem 84(4):338–44
- Varsano N, Beghi F, Elad N, Pereiro E, Dadosh T, et al. 2018. Two polymorphic cholesterol monohydrate crystal structures form in macrophage culture models of atherosclerosis. PNAS 115(30):7662–69
- Schneider G, Guttmann P, Heim S, Rehbein S, Mueller F, et al. 2010. Three-dimensional cellular ultrastructure resolved by X-ray microscopy. Nat. Methods 7(12):985–87
- Hagen C, Guttmann P, Klupp B, Werner S, Rehbein S, et al. 2012. Correlative VIS-fluorescence and soft X-ray cryo-microscopy/tomography of adherent cells. J. Struct. Biol. 177(2):193–201
- 136. Hagen C, Werner S, Carregal-Romero S, N Malhas A, G Klupp B, et al. 2014. Multimodal nanoparticles as alignment and correlation markers in fluorescence/soft X-ray cryo-microscopy/tomography of nucleoplasmic reticulum and apoptosis in mammalian cells. *Ultramicroscopy* 146:46–54
- Elgass KD, Smith EA, LeGros MA, Larabell CA, Ryan MT. 2015. Analysis of ER-mitochondria contacts using correlative fluorescence microscopy and soft X-ray tomography of mammalian cells. J. Cell. Sci. 128(15):2795–804
- Linklater DP, Le Guével X, Kosyer E, Rubanov S, Bryant G, et al. 2023. Functionalized gold nanoclusters promote stress response in COS-7 cells. Adv. NanoBiomed. Res. 3(4):2200102
- 139. Schneider G. 1998. Cryo X-ray microscopy with high spatial resolution in amplitude and phase contrast. *Ultramicroscopy* 75(2):85–104
- 140. Uchida M, McDermott G, Wetzler M, LeGros MA, Knoechel C, et al. 2009. Soft X-ray tomography of phenotypic switching and the cellular response to antifungal peptoids in *Candida albicans. PNAS* 106:19375–80